University of Bath

Alternative formats
If you require this document in an alternative format, please contact:
openaccess@bath.ac.uk

Revealing the Influence of Doping and Surface Treatment on the Surface Carrier Dynamics in Hematite Nanorod Photoanodes

Gurudayal,[b,c] Laurence M. Peter,[d] Lydia H. Wong,*[b] and Fatwa F. Abdi*[a]

[a] Institute for Solar Fuels Helmholtz-Zentrum Berlin für Materialien und Energie GmbH, Hahn-Meitner-Platz 1, Berlin 14109, Germany

[b] School of Materials Science and Engineering, Nanyang Technological University, Nanyang Avenue, Singapore 639798

[c] Joint Center for Artificial Photosynthesis, Lawrence Berkeley National Laboratory, 1 Cyclotron Road, Berkeley, CA 94720, USA

[d] Department of Chemistry, University of Bath, Bath BA2 7AY, United Kingdom

ABSTRACT: Photoelectrochemical (PEC) water oxidation is considered to be the rate-limiting step of the two half-reactions in light-driven water splitting. Consequently, considerable effort has focused on improving the performance of photoanodes for water oxidation. While these efforts have met with some success, the mechanisms responsible for improvements resulting from photoanode modifications are often difficult to determine. This is mainly caused by the entanglement of numerous properties that influence the PEC performance, particularly processes that occur at the photoanode/electrolyte interface. In this study, we set out to elucidate the effects on the surface carrier dynamics of hematite photoanodes of introducing manganese (Mn) into hematite nanorods and of creating a core-shell structure. Intensity-modulated photocurrent spectroscopy (IMPS) measurements reveal that the introduction of Mn into hematite not only increases the rate constant for hole transfer but also reduces the rate constant for surface recombination. In contrast, the core-shell architecture evidently passivates the surface states where recombination occurs; no change is observed for the charge transfer rate constant, whereas the surface recombination rate constant is suppressed by ~1 order of magnitude.

Introduction

Photoelectrochemical (PEC) water splitting is an attractive way to overcome the intermittency of sunlight by storing solar energy in the form of chemical fuels.[1-5] However, progress in obtaining highly-efficient PEC performance has been limited by the availability of suitable photoanode materials for the water oxidation half reaction.[6-9] In the last decade, TiO_2,[10-11] $BiVO_4$,[12-13] WO_3[14] and Fe_2O_3[15-19] have been used extensively as photoanodes for PEC water oxidation. However, the water splitting efficiency obtained with these oxides is still far below the theoretical maximum efficiency. The efficiency losses have been attributed to factors such as poor electronic transport and low hole transfer efficiency due to competition from surface recombination.[20-23] These losses are particularly evident in the case of hematite (Fe_2O_3). Despite being an economically viable, corrosion-resistant semiconductor with a suitable bandgap energy for carrying out the visible-light induced oxygen evolution reaction,[18, 23-25] the short hole diffusion lengths and sluggish kinetics of hole transfer limit the performance of hematite. In particular, the short hole diffusion length, combined with the fact that hematite's optical penetration depth is larger than the depletion layer width,[26-27] means that a significant fraction of the photogenerated charge carriers does not reach the surface and instead recombines in the bulk. Despite the valence band energy of hematite being thermodynamically favorable (i.e., ~1.2 eV below the redox Fermi level for the O_2/H_2O couple), photogenerated holes that arrive at the hematite/electrolyte interface are transferred with a very low efficiency unless high positive potentials are applied.[28] This indicates that the kinetics of hole transfer for oxygen evolution in hematite is so slow that holes are lost through surface recombination unless high bias potentials are used to lower the electron concentration in the surface region.

The problems mentioned above have been overcome to a certain extent by means of various strategies. The mismatch of optical penetration and carrier transport has been addressed by nanostructuring on a scale comparable with or smaller than the width of the space charge region, thereby increasing the probability of holes reaching the electrode/electrolyte interface before recombining in the bulk. At the same time, nanostructuring greatly improves the light-harvesting efficiency of electrodes because it removes the geometric restriction on the direction of illumination relative to the orientation of the space charge region, which is orthogonal for plane electrodes.[29] Significant improvements in the performance of hematite photoanodes have also been achieved through doping (e.g., with Mn, Sn, Ti, Si),[30-32] although the mechanisms responsible are generally unclear. Finally, attempts have been made to address kinetic limitations by depositing a so-called 'co-catalyst' layer onto the surface of hematite (e.g., CoO_x, SnO_x, TiO_x, CoPi and IrO_2).[11, 24, 33-36] These approaches have often been combined in order to obtain improved performance in hematite photoanodes. For example, in our previous work, we synthesized Mn-doped, core-shell, and nanorod-structured hematite layers in order to overcome the poor carrier transport, the sluggish kinetics, and the short hole diffusion length, respectively.[37-38] As a result, we obtained a factor of three improvement as compared to a bare hematite film with much lower degree of porosity. However, the exact mechanisms giving rise to the observed improvement arising from the above-mentioned modifications were not clear. Understanding the enhancement mechanisms will arguably bring us closer to achieving the theoretically predicted maximum solar-to-hydrogen conversion efficiency of 15%, assuming that all photons in the AM 1.5G solar spectrum that have energy larger than the energy bandgap of hematite can be collected and converted to photocurrent without additional external bias.[10, 25, 39]

Here, we attempt to shed light on the improvement mechanisms by performing systematic intensity-modulated photocurrent spectroscopy (IMPS) measurements. IMPS allows de-convolution of charge carrier dynamics at the electrode/electrolyte interface into contributions from charge transfer and surface recombination. It is an increasingly attractive technique for understanding surface carrier dynamics at the semiconductor/electrolyte interface.[40-43] In the present study, we investigated the effect of Mn doping and of a thin shell layer of highly crystalline Fe_2O_3 on hydrothermally grown hematite nanorods. Our data reveal that although the photocurrent enhancements achieved by each type of modifications are similar, the causes are inherently different. In particular, the photocurrent enhancement observed in Mn-doped hematite can be explained by the increase in surface charge transfer efficiency, which is typically not expected for a bulk modification such as doping. Overall, our results provide further insights of the role of doping and surface modification in hematite, and may form the basis of future improvement strategies.

Experimental Section

Nanorod synthesis

Pristine, Mn-doped and core–shell hematite nanorod samples were grown on a fluorine-doped tin oxide (FTO) substrate (Pilkington TEC-15, Ω < 14 ohm/square). The Fe_2O_3 nanorods were synthesized hydrothermally as reported in our previous reports,[37-38] with one modification: the hydrothermal synthesis was carried out only for 6 hours, instead of the reported 10 hours. In short, after 6 h of hydrothermal synthesis at 100 °C, a uniform layer of FeOOH nanorods film was formed on the FTO substrate. The FeOOH samples were carefully rinsed with distilled water and subsequently annealed at 550 °C for 2 hours to form hematite. The Mn-doped hematite nanorods were prepared using a similar method as the pristine hematite with the addition of 5 mol % of $MnCl_2 \cdot 4H_2O$ ($\geq$ 98%, Sigma-Aldrich) to the precursor solutions. In the case of core-shell hematite samples, 0.1 M iron acetylacetonate (97%, Sigma-Aldrich) precursor in ethanol was sprayed onto the hydrothermal synthesized FeOOH nanorods placed on a hot plate at 525 °C, using a home-built spray pyrolysis setup. The spray step was done for 4 cycles with each cycle consisting of 20 seconds of

spraying time, which is followed by an annealing treatment at 550 °C in air. The distance between the spray head and the hematite sample was kept at 20 cm. Finally, all samples (pristine, Mn-doped and core–shell hematite) were heated at 750 °C in air for 20 min.

Characterization methods

X-ray diffraction patterns of pristine, Mn-doped and core-shell hematite samples collected over a two-theta value range from 20 to 60 degrees were carried out with Shimadzu instrument (Lab X, XRD-6000) in a Bragg-Brentano configuration at an accelerating voltage of 40 kV, a current of 30 mA and a scan speed of 2 degree/minute. The surface morphology of the samples was characterized by field-emission scanning electron microscopy (FESEM JEOL, JSM-7600F, 5kV). Secondary ions mass spectrometry (SIMS) depth profiles were attained using a TOFSIMS IV instrument from IONTOF (GmbH). An Ar^+ ion beam of 3 keV was used for sputtering and a pulsed Bi^+ ion beam of 25 keV was utilized for analysis with detection of positive secondary ions. An electron flood gun was employed for charge compensation. The ultraviolet-visible (UV-Vis) absorption spectra of the pristine, Mn-doped and core-shell hematite samples were obtained using a Perkin-Elmer Lambda 750S UV-Vis-NIR spectrophotometer equipped with an integrated sphere with a diameter of 60 mm. PEC measurements were performed using CHI 660D working station potentiostat (CH Instruments, Inc.) in a three-electrode electrochemical cell filled with 1 M NaOH (pH=13.6) electrolyte. A platinum coil and a Ag/AgCl electrode (Chi 111, saturated in 3M KCl) were employed as counter and reference electrodes, respectively. The working surface area was 0.12 cm². The light source was a 150 W xenon lamp (67005, Newport Corp.) equipped with a solar filter (KG 3). The measured illumination intensity is adjusted to standard AM 1.5G sunlight (100 mWcm⁻²) on the sample surface.

IMPS measurements of pristine, Mn-doped and core-shell hematite photoanodes were conducted using a potentiostat (EG&G 283, Princeton Applied Research) in a three-electrode configuration with a Ag/AgCl reference electrode (XR300, saturated KCl and AgCl solution, Radiometer Analytical), and a platinum wire counter electrode. The electrolyte was 1 M NaOH. Modulated illumination was provided by a light-emitting diode (LED, λ: 455 nm, Thorlabs) controlled by an LED driver (Thorlabs DC 2100) that allowed superimposition of sinusoidal modulation (0.6 mW/cm²) on a dc illumination level (4 mW/cm²). A frequency response analyzer (Solartron 1250) was used to supply both the dc and ac signals to the LED driver. The LED illumination is then directed towards a beam-splitter, which splits the light into two paths: a high-speed silicon pin photodiode (Thorlabs PDA10A-EC) to measure the light intensity, and the hematite sample in a photoelectrochemical cell. The modulated photocurrent and the reading of the pin photodiode were then fed back to the channel 1 and 2 of the frequency response analyzer, respectively. The measured complex data (channel 1/channel 2) is then post-processed according to

the procedures described in the next section to obtain a normalized complex photocurrent current plot.

IMPS Theory

Illumination of a semiconductor-electrolyte junction generates photo-excited carriers (electrons in the conduction band and holes in the valence band). If the generation occurs within the depletion layer, these electrons and holes will be separated efficiently due to the gradients of the respective quasi-Fermi levels. For an n-type semiconductor, such as hematite, electrons will move to the back contact, and holes will move to the semiconductor/electrolyte interface. In addition, there is a diffusion flux associated with holes that are generated within a diffusion length of the edge of the space charge region. Together with the flux of holes generated in the space charge region, this constitutes the hole current (j_{hole}), i.e., the rate at which holes arrive at the semiconductor/electrolyte interface (here we assume that the assumptions of the Gärtner model[44] assumption are valid, i.e., we neglect space charge recombination). The processes at the semiconductor/electrolyte interface are illustrated in Figure 1a, based on the model proposed by Peter and co-workers.[45-47] The photo-generated holes reaching the interface can either transfer to the electrolyte to oxidize water (in a 4-electron oxidation process) or recombine with the electrons from the conduction band via surface states. Note that, in Fig. 1, we show hole transfer to the electrolyte as occurring via the surface states. This is not necessarily the case; hole transfer directly from the valence band is also possible, but this does not change the kinetic analysis significantly.

A commonly used dynamic photoelectrochemical method used to probe the dynamics of photoelectrochemical processes is transient photocurrent measurement. The sample is subjected to chopped illumination at a constant potential, and the resulting photocurrent is monitored. A typical transient photocurrent response is shown in Figure 1b. The instantaneous photocurrent in the transient corresponds to the displacement current caused by holes charging the space charge capacitance. This current defines the rate at which holes arrive at the surface (j_{hole}), but not the rate at which they transfer across the interface. At longer times, interfacial charge transfer and surface recombination occur, and the photocurrent decays to the steady-state photocurrent (j_{ss}), which is equal to the hole current into the surface minus the recombination current. The resulting hole transfer efficiency at the semiconductor/electrolyte interface is therefore the ratio of the steady state photocurrent (j_{ss}) to the instantaneous photocurrent (j_{hole}). If we assume that hole transfer and surface recombination reactions are first order (or more precisely pseudo-first order for a constant potential - where the concentration of electrons at the surface is constant - and for constant concentration of oxidation species), the hole transfer efficiency can be expressed in terms of the hole transfer (k_{tr}) and surface recombination (k_{rec}) rate constants:

$$\eta_{tr} = \frac{j_{ss}}{j_{hole}} = \frac{k_{tr}}{k_{tr} + k_{rec}} \qquad (1)$$

Here, k_{tr} is expected to be independent of potential in the absence of changes in the potential drop across the Helmholtz layer, whereas k_{rec} is potential-dependent because it depends linearly on the concentration of majority carriers (electrons) at the surface (see below).

Unfortunately, transient photocurrent measurements may be influenced by the processes other than hole transfer and surface recombination. The large difference between dark and illuminated conditions may cause changes in band bending and/or significant population or depopulation of surface states. The corresponding light-induced changes in the potential distribution across the junction may affect the rate constants, and complicate the analysis of the data. This is much less of a problem in intensity modulated photocurrent spectroscopy (IMPS) because a small amplitude (~10%) sinusoidal modulation of light intensity is applied on top of a constant dc value. This modulation results in a change in phase and amplitude (i.e., real and imaginary component) of the photocurrent. This photocurrent response to intensity-modulated illumination as a function of frequency results in semicircles in the complex plane, as shown in Figure 1c. The complex normalized photocurrent (j_{photo}/j_{hole}) is obtained by normalizing our frequency response analyzer reading so that the crossing point on the real-axis is equal to unity. This is done because in the absence of significant RC attenuation, the crossing point represents the total number of holes that arrives at the semiconductor/electrolyte interface (i.e., hole current).[46] The assumption is valid if the space charge capacitance (C_{SC}) is much lower than the Helmholtz capacitance (C_H), which is true for the case of our hematite samples (C_{SC} is ~1-2 orders of magnitude smaller than C_H).

The lower quadrant semicircle represents the attenuation by the total series resistance of the photoelectrochemical cell and the capacitances of the sample, typically referred to as the RC time constant of the cell.[48] Of more particular interest to us, is the upper quadrant semicircle, also referred

to as the recombination semicircle. The first order rate constants k_{tr} and k_{rec} can be obtained by analyzing this semicircle. The high and low frequency intercepts in the complex plane correspond in the time domain to the steady state and instantaneous photocurrents in the transient photocurrent measurement. The ratio of the low and high frequency intercepts therefore corresponds to the hole transfer efficiency (see eq. 1). The maximum of the semicircle occurs at a radial frequency that is equal to the sum k_{tr} and k_{rec}, i.e., the characteristic relaxation constant of the system. Based on these values, both k_{tr} and k_{rec} can be calculated. The first-order rate constants k_{rec} can be further expressed in terms of the thermal velocity (v) and capture cross-section (σ) of the surface majority carrier concentration (n_{surf}):

$$k_{rec} = v \times \sigma \times n_{surf} \qquad (2)$$

$$n_{surf} = n_{bulk} e^{-\frac{q\Delta\phi}{kT}} \qquad (3)$$

n_{bulk} is the bulk majority carrier concentration, q is elementary charge, $\Delta\phi$ is the potential drop within the space charge layer, k is Boltzmann constant, and T is temperature in Kelvin. Further detailed explanations of the model and interpretation of IMPS measurements can be found in the literature.[41, 49-50]

We finally note that caution should be exercised when interpreting the value of the rate constants described above. For a simple one-electron charge transfer reaction, these rate constants are true rate constants (s^{-1}). This is however not the case for multi-step charge transfer reactions such as the 4-electron oxidation of water. The same expressions to analyze the IMPS response and distinguish the hole transfer and surface recombination processes can still be used, but k_{tr} and k_{rec} are now to be interpreted as phenomenological rate parameters that are functions of the rate constants of the elementary steps.[51-52] In principle, these functional expressions can be derived if the reaction mechanism is known,[51] but so far this has not been attempted for the photo-oxidation of water. In this work, we therefore consider k_{tr} and k_{rec} as phenomenological pseudo first-order rate constants.
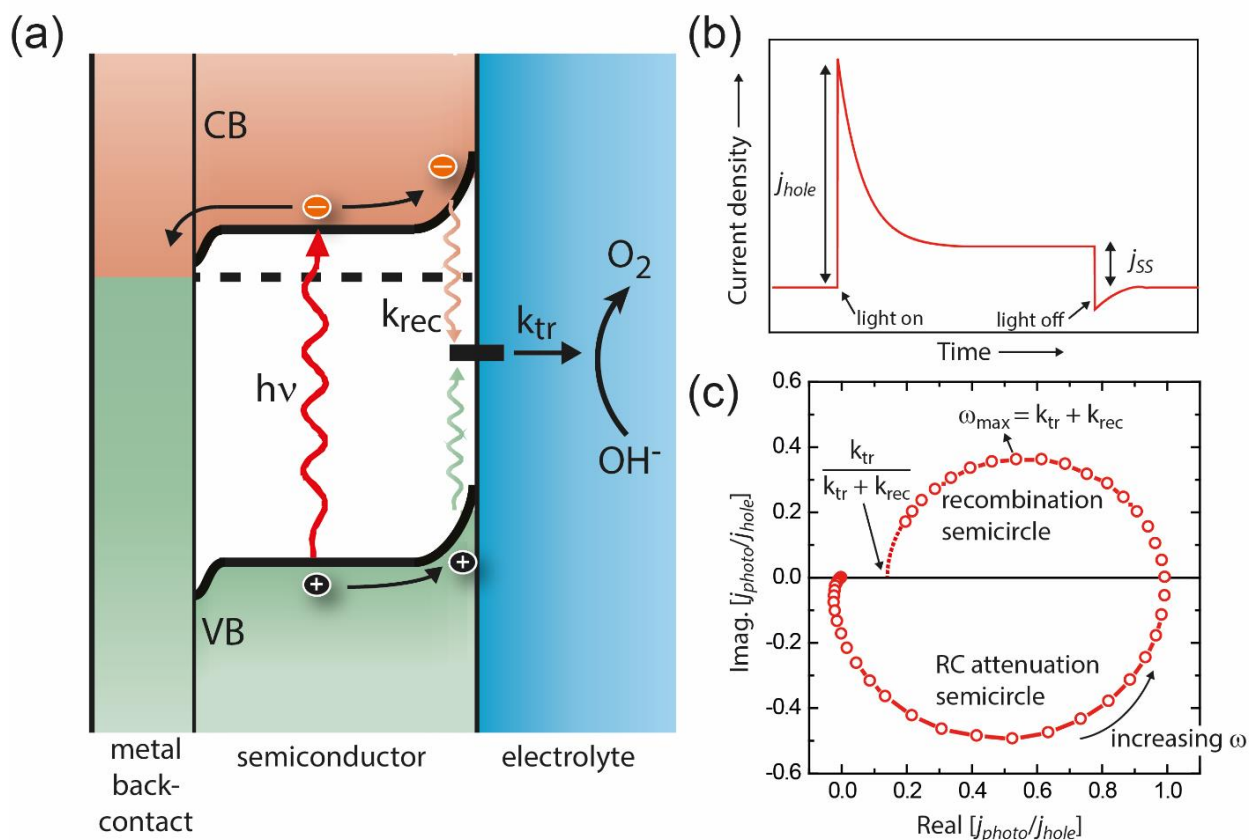
Figure 1. (a) Schematic of competition between charge transfer and recombination. k_{tr} and k_{rec} are the pseudo first order rate constants for charge transfer and surface recombination, respectively. (b) A typical photocurrent transient of an n-type semiconductor immersed in an electrolyte, under chopped illumination. (c) A typical example of complex photocurrent or IMPS spectrum. The semicircle in upper quadrant corresponds to the competition between charge transfer and recombination, and the semicircle in the lower quadrant is due to the RC attenuation of the system.

Results and Discussion

As mentioned above, we are interested in the mechanisms responsible for the photocurrent increase in hematite photoanodes. Specifically, Mn doping and the deposition of a highly crystalline shell layer, which we have shown to significantly improve the photocurrent of our hematite nanorods,[30] are investigated. Figure 2 illustrates these improvements in the AM1.5 photocurrent-voltage characteristics. While the pristine hematite shows an AM1.5 photocurrent density of ~0.5 mA cm^{-2} at 1.23 V vs RHE and an onset potential of ~1.0 V vs RHE—typical for an undoped hematite—both Mn doping and core-shell modification results in a twofold enhancement of the photocurrent as well as a cathodic shift of onset potential by ~200 mV. The XRD patterns of the hydrothermally grown pristine, Mn-doped and core-shell hematite photoanodes could be seen in our previous reports, which clearly show that there is no significant difference in the XRD pattern after Mn doping and core-shell modification.[37-38] Top and cross section view SEM images of all samples (Supporting Figure S1) show that the nanorod geometry is maintained, and the radii of the core-shell hematite nanorods are slightly larger, as expected.

Supporting Figure S2 shows the UV-vis absorption spectra of pristine, Mn-doped and core-shell hematite photoanodes, indicating that no distinct differences in features can be observed between these different samples. The optical indirect band gaps of all samples, extracted from Tauc analyses (Supporting Figure S3), show a consistent value of 2.05 ± 0.02 eV. Overall, we observed no significant difference in structural and optical properties between the pristine, Mn-doped and core-shell hematite photoanodes—consistent with our previous reports[30, 37-38]—thereby ruling out structural or optical effects as the cause of the observed photocurrent improvement.

Photocurrent transient measurements were performed in order to provide preliminary characterization of the surface carrier dynamics at the pristine, Mn-doped and core-shell hematite-electrolyte interface under AM1.5G illumination (Supporting Figure S4). The decay and overshoot in the photocurrent transients is less for the Mn-doped and core-shell hematite photoanodes compared to the pristine sample, which indicates better charge transfer efficiency to the electrolyte. However, based on this data, it is not possible to

5

identify whether the observed enhancement is due to reduction of surface recombination or to improvement of charge transfer, or to both.
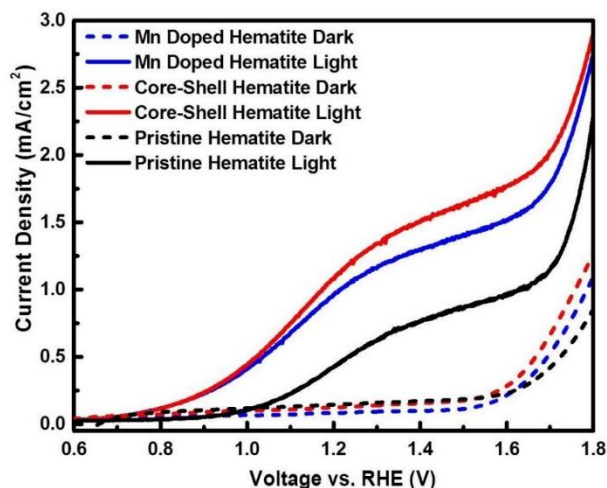

Figure 2. Photocurrent-potential curve of pristine, Mn-doped and core-shell hematite photoanodes measure under AM 1.5G (100 mWcm⁻²) in 1M NaOH electrolyte solution.

To understand the interplay between charge transfer and surface recombination processes in these hematite nanorod samples, we measured their IMPS responses over a potential range of 0.6 V to 1.3 V vs. RHE. Figure 3 contrasts the complex IMPS responses of pristine (black) and core-shell (red) hematite nanorods, measured at 1.0 V vs RHE. As explained

in the theory section, the low-frequency semicircle (upper quadrant) can be used to de-convolute the charge transfer and surface recombination rate constants. The smaller radii of the semicircles for the Mn-doped and core-shell hematite samples (i.e., higher hole transfer efficiency) as compared to the pristine one is consistent with the photocurrent improvement observed in the photocurrent-voltage curves (Figure 2).
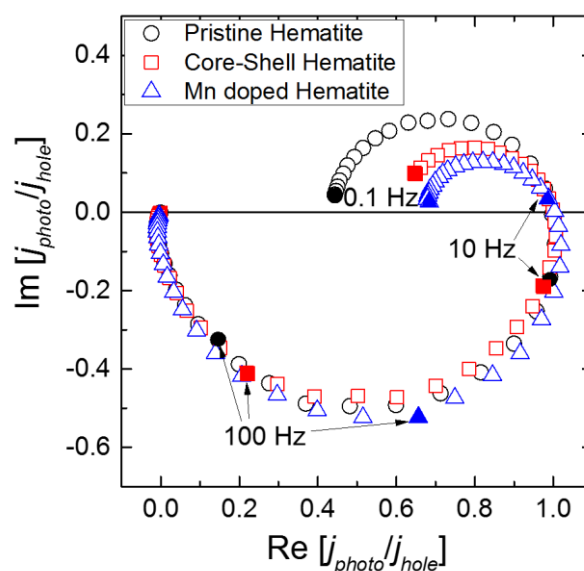

Figure 3. IMPS spectra of pristine, Mn-doped and core-shell hematite samples measured at 1.0 V vs. RHE under blue LED (λ = 455 nm) illumination in 1M NaOH electrolyte solution.
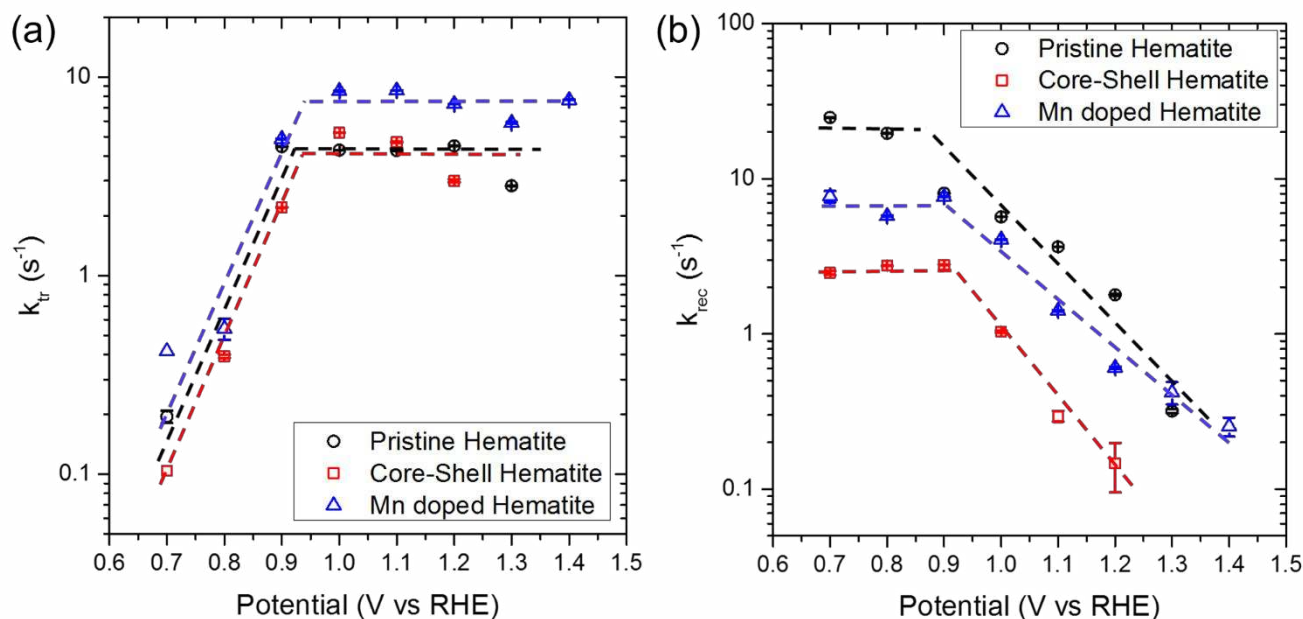

Figure 4. (a) Charge transfer rate constant k_{tr} and **(b)** surface recombination rate constant k_{rec} of pristine, Mn-doped and core-shell hematite samples as a function of potential. Dashed lines are meant as guide to the eye, and not linear fit of the data.

6

The charge transfer (k_{tr}) and surface recombination (k_{rec}) rate constants calculated for the pristine and core-shell hematite at different potentials are shown in Figure 4a and b (black and red curves, respectively). Two potential regimes can be distinguished for both hematite samples. For potentials lower than 0.9 V vs. RHE, k_{tr} increases with increasing potentials, while k_{rec} remains relatively constant. This behavior indicates Fermi level pinning on the surface of hematite; changes in applied potential do not modify the band bending but instead increase the potential drop across the Helmholtz layer and hence increase k_{tr} in the same way as at a metal electrode. Above 0.9 V vs. RHE, the hematite behaves more like a 'normal' semiconductor, i.e., k_{tr} remains constant and k_{rec} decreases with increasing potential. This indicates saturation of the surface state occupancy as expected for a surface state distribution centered on a discrete energy.

Figures 4a and b show that both the pristine and core-shell hematite have relatively similar k_{tr} values. However, the core-shell hematite has ~1 order of magnitude lower k_{rec} as compared to the pristine sample for the entire potential range. This observation indicates that the core-shell architecture is effective in improving the photocurrent by suppressing surface recombination, rather than by increasing charge transfer. The surface of the pristine hematite evidently has a large number of surface states,[53] which may act as recombination centers. Deposition of a highly-crystalline shell layer (see SAED pattern and TEM images, Supporting Figure S5, as well as our previous report[37]) appears to—at least partially—passivate these surface states, possibly by decreasing their capture cross section (cf. eq. 2 in the theory section), which in turn reduces surface recombination. The photocurrent enhancement for the core-shell hematite (Fig. 2) is therefore mainly caused by this suppression of recombination.

We now turn our attention to the Mn-doped hematite sample. The IMPS spectrum obtained at 1.0 V vs. RHE for the Mn-doped hematite is shown in Figure 3 (blue). Similar to the core-shell hematite, the radius of the low-frequency semicircle (upper quadrant) of the Mn-doped hematite is also decreased as compared to the pristine hematite. Based on the IMPS responses, the potential dependent rate constants, k_{tr} and k_{rec}, for the Mn-doped hematite were calculated (Figure 4a & b, blue). At high potentials (> 0.9 V vs. RHE), the Mn-doped hematite shows ~2-fold improvement of k_{tr} as compared to the pristine hematite (Fig. 4a), while k_{rec} is relatively unchanged (Fig. 4b). This means that introducing Mn into hematite improves surface hole transfer kinetics. While this is rather unexpected, a similar observation has also been reported in the case of Sn-doped hematite by Dunn et al.,[40] who demonstrated that Sn-enrichment at the surface improved the catalytic properties at the surface. To establish whether this is also the case in our Mn-doped hematite, we performed Mn-depth profile measurement using secondary ion mass spectroscopy (SIMS), as shown in Figure 5. While the enrichment is not as high as the report on Sn-doped hematite, it is clear that the amount of Mn is higher at the surface as compared to the bulk. We

believe that this is the main reason behind the enhancement of hole transfer rate constant. The multivalent oxidation states of manganese possibly leads to a low (O-Mn-O) energy barrier for hole transfer, and improves the OER activity of hematite photoanode.[54] Indeed, we have shown recently that the decoration of the surface of hematite with MnO nanocrystals resulted in increased hole transfer rate constant.[55]
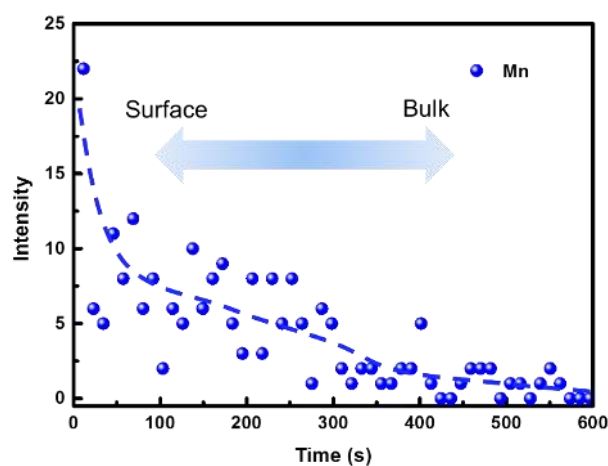

Figure 5. Depth intensity (counts) profile of Mn in the Mn-doped hematite measured with Secondary Ion Mass Spectroscopy (SIMS). Shorter time corresponds to the surface of the sample, while the bulk of the sample is probed at longer time.

The effect of Mn doping on k_{tr} and k_{rec} is different at lower applied potentials (< 0.9 V vs RHE). While the k_{tr} values are similar for Mn-doped and pristine hematite, the k_{rec} values decrease by a factor of ~2-3 (Fig. 4a and b). This is in contrast to the Sn-doped hematite, where the krec values were instead reported to increase upon Sn-doping.[40] We note that Mn^{4+} has an ionic radius of 53 pm, which is very close to that of Fe^{3+} (55 pm). This is not the case for Sn^{4+} (69 pm), which may introduces higher degree of defects.

According to eq. 2 and 3 in the Theory section, k_{rec} is proportional to the surface majority concentration (n_{surf}), which is proportional at any given band bending to the donor density (n_{bulk}). We have previously reported ~2 orders of magnitude increase of donor density for the Mn-doped hematite as compared to the pristine.[30] While the observed trend of increasing carrier concentration may be true, using a typical flat electrodes Mott-Schottky analysis for nanorod geometries can result in a significant error. Here, a more accurate cylindrical model was used to fit the Mott-Schottky curves of both pristine and Mn-doped hematite (Figure 6a and b, see Supplementary information for full details of the model). It can be seen that application of the standard Mott-Schottky approach to the nanorod geometry results in a gross underestimation of the donor density, particularly in the case of the undoped hematite. Nevertheless, the analysis confirms that Mn doping results in a much higher n_{bulk}, which would be expected to increase k_{rec}. Since this increase

7

is not observed experimentally, we speculate that the presence of Mn on the surface of our hematite results in the passivation of surface states, possibly by the formation of a thin MnO_x layer on the surface. We have attempted to detect this by performing x-ray photoelectron spectroscopy (XPS), but the small amount of Mn is below the resolution of our measurement. Further experiments beyond the scope of this paper are needed in order to confirm this suggestion.

We note that the positive shift of flatband potential upon Mn-doping (Figure 6) is rather unexpected. Doping increases carrier concentration, which in turn raises the Fermi level closer to the conduction band. One would then expect the flatband potential to shift negatively. However, the same positive shift has been reported in many other systems based on doped-hematite and doped-bismuth vanadate.[56-59]
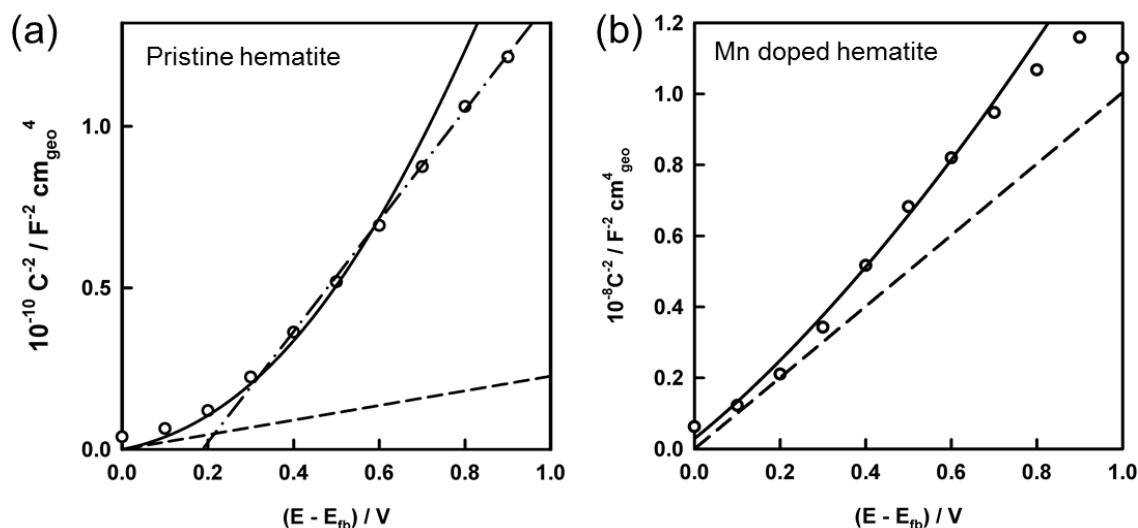

Figure 6. Mott Schottky plots for **(a)** pristine and **(b)** Mn-doped Fe_2O_3 nanorod electrodes. Open circles – experimental. Curve – fit for an array of cylindrical rods on an FTO substrate. Dashed straight line – Mott Schottky plot for flat electrode with same area and doping density. Dash-dot line - linear fit of experimental data ignoring effect of cylindrical geometry. Note that the linear fit grossly underestimates the doping density and gives an incorrect value of the flatband potential. Fit parameter: rod density 3.5×10^{10} cm^{-1}, rod length 350 nm, mean rod radius 25 nm, packing fraction 70%, and relative permittivity of $Fe_2O_3 = 33$.[60] For full details of the model and fitting see Supporting Information. The obtained doping density and flatband potential for the pristine hematite are 5.1×10^{18} cm^{-3} and 0.3 V vs RHE, respectively. The values for the Mn-doped hematite are 1.15×10^{20} cm^{-3} and 0.5 V vs RHE, respectively.
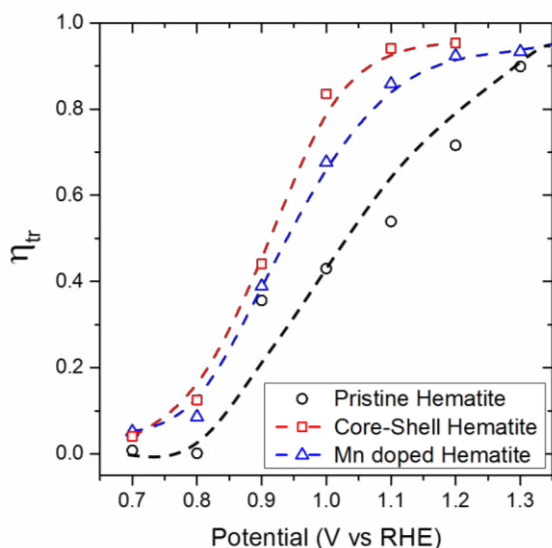
Figure 7. Charge transfer efficiency (η_{tr}) of pristine, core-shell and Mn-doped hematite as a function of applied potential. Dashed lines are guide to the eye.

Figure 7 shows the charge transfer efficiency (η_{tr}, defined as $k_{tr}/k_{tr}+k_{rec}$) as a function of potential for all the hematite samples: pristine, core-shell and Mn-doped. Although the improvement mechanisms (i.e., the k_{tr} and k_{rec} values) for core-shell and Mn-doped hematite are different, the overall charge transfer efficiencies are similarly improved as compared to the pristine hematite. The calculated enhancement in charge transfer efficiency is also consistent with the photocurrent improvement and the cathodic shift of onset potential shown in the photocurrent-voltage curves (Figure 2), which further validates our IMPS measurement and analysis. For the Mn-doped and core-shell hematite, the photocurrent in Fig. 2 continues to increase beyond 1.1 V vs RHE, although the charge transfer efficiencies are already close to one. This suggests that the space charge region is smaller than the radius of the nanorods. Based on the Mott-Schottky plot (Figure 6), we obtained a carrier concentration of 5.1×10^{18} and 1.1×10^{20} cm^{-3} for the pristine and Mn-doped hematite, respectively. These values result in respective space charge widths of 20 and 4.7 nm (at band bending of 1 eV). These values are indeed smaller than the radius of the nanorods (~25 nm). The much smaller space charge width for the Mn-doped hematite does not seem to negatively influence the photocurrent, since the main limiting factor is surface charge transfer.

Finally, we note that although the charge transfer efficiencies shown in Figure 7 have reached a value of close to unity at high applied potentials, the photocurrent is still much lower than the theoretical maximum. Since only surface processes were considered in our analysis, this means that the performance of hematite for water oxidation is limited by fast recombination of carriers either in the quasi neutral region, the space charge layer, or both. Future efforts on hematite, if one chooses to work on it, should therefore focus on bulk modification and not only directed to the surface modifications.

Conclusions

In conclusion, we have investigated the effect of Mn doping and core-shell architecture to the surface carrier dynamics of hematite. We have shown that despite the similar improvement of both modifications of hematite in the AM1.5 photocurrent, the actual mechanisms of the improvement are not the same. Surprisingly, doping with Mn results in a 2-fold increase of the hole transfer rate constant. Despite doping being normally considered as a bulk modification, the higher concentration of Mn at the surface of our hematite (as shown by SIMS measurement) also increases the catalytic activity. This observation has also been shown for Sn doping in hematite.[40] In contrast, the core-shell architecture does not affect the hole transfer rate constant; instead it reduces the surface recombination rate constant by ~one order of magnitude. These different enhancements are the main reason for the observed increased AM1.5 photocurrent. Finally, we have demonstrated the capability of IMPS to analyze and provide insights into the surface carrier dynamics of photoelectrode materials for solar water oxidation.

ASSOCIATED CONTENT

Supporting Information. Figure S1-9, Table S1 and Supplementary Note. This material is available free of charge via the Internet at http://pubs.acs.org.

AUTHOR INFORMATION

Corresponding Author

fatwa.abdi@helmholtz-berlin.de, lydiawong@ntu.edu.sg

## REFERENCES

1. Ohashi, K.; McCann, J.; Bockris, J. O. M., Stable photoelectrochemical cells for the splitting of water. *Nature* **1977**, *266*, 610-611.
2. Bard, A. J.; Fox, M. A., Artificial Photosynthesis: Solar Splitting of Water to Hydrogen and Oxygen. *Acc. Chem. Res.* **1995**, *28*, 141-145.
3. Coridan, R. H.; Shaner, M.; Wiggenhorn, C.; Brunschwig, B. S.; Lewis, N. S., Electrical and

photoelectrochemical properties of WO_3/Si tandem photoelectrodes. *J. Phys. Chem. C* **2013,** *117*, 6949-6957.

4. Walter, M. G.; Warren, E. L.; McKone, J. R.; Boettcher, S. W.; Mi, Q.; Santori, E. A.; Lewis, N. S., Solar water splitting cells. *Chem. Rev.* **2010,** *110*, 6446-6473.

5. Tachibana, Y.; Vayssieres, L.; Durrant, J. R., Artificial photosynthesis for solar water-splitting. *Nat. Photon.* **2012,** *6*, 511-518.

6. Nocera, D. G., The artificial leaf. *Acc. Chem. Res.* **2012,** *45*, 767-776.

7. Jeon, N. J.; Noh, J. H.; Kim, Y. C.; Yang, W. S.; Ryu, S.; Seok, S. I., Solvent engineering for high-performance inorganic–organic hybrid perovskite solar cells. *Nat. Mater.* **2014,** *13*, 897-903.

8. Mayer, M. T.; Lin, Y.; Yuan, G.; Wang, D., Forming Heterojunctions at the Nanoscale for Improved Photoelectrochemical Water Splitting by Semiconductor Materials: Case Studies on Hematite. *Acc. Chem. Res.* **2013,** *46*, 1558-1566.

9. Chen, Y. W.; Prange, J. D.; Dühnen, S.; Park, Y.; Gunji, M.; Chidsey, C. E. D.; McIntyre, P. C., Atomic layer-deposited tunnel oxide stabilizes silicon photoanodes for water oxidation. *Nat. Mater.* **2011,** *10*, 539-544.

10. Fujishima, A.; Honda, K., Electrochemical photolysis of water at a semiconductor electrode. *Nature* **1972,** *238*, 37-38.

11. Tsui, L. K.; Zangari, G., The influence of morphology of electrodeposited Cu_2O and Fe_2O_3 on the conversion efficiency of TiO_2 nanotube photoelectrochemical solar cells. *Electrochim. Acta* **2013,** *100*, 220-225.

12. Abdi, F. F.; Han, L.; Smets, A. H. M.; Zeman, M.; Dam, B.; van de Krol, R., Efficient solar water splitting by enhanced charge separation in a bismuth vanadate-silicon tandem photoelectrode. *Nat. Commun.* **2013,** *4:2195*, 1-7.

13. McDonald, K. J.; Choi, K.-S., Synthesis and Photoelectrochemical Properties of Fe_2O_3/$ZnFe_2O_4$ Composite Photoanodes for Use in Solar Water Oxidation. *Chem. Mater.* **2011,** *23*, 4863-4869.

14. Dias, P.; Lopes, T.; Meda, L.; Andrade, L.; Mendes, A., Photoelectrochemical water splitting using WO_3 photoanodes: the substrate and temperature roles. *Phys. Chem. Chem. Phys.* **2016,** *18*, 5232-5243.

15. Gurudayal; Sabba, D.; Kumar, M. H.; Wong, L. H.; Barber, J.; Grätzel, M.; Mathews, N., Perovskite–Hematite Tandem Cells for Efficient Overall Solar Driven Water Splitting. *Nano Lett.* **2015,** *15*, 3833-3839.

16. Kay, A.; Cesar, I.; Grätzel, M., New benchmark for water photooxidation by nanostructured α-Fe_2O_3 films. *J. Am. Chem. Soc.* **2006,** *128*, 15714-15721.

17. Dotan, H.; Kfir, O.; Sharlin, E.; Blank, O.; Gross, M.; Dumchin, I.; Ankonina, G.; Rothschild, A., Resonant light trapping in ultrathin films for water splitting. *Nat. Mater.* **2013,** *12*, 158-164.

18. Warren, S. C.; Voïtchovsky, K.; Dotan, H.; Leroy, C. M.; Cornuz, M.; Stellacci, F.; Hébert, C.; Rothschild, A.; Grätzel, M., Identifying champion nanostructures for solar water-splitting. *Nat. Mater.* **2013,** *12*, 842-849.

19. Lin, Y.; Yuan, G.; Sheehan, S.; Zhou, S.; Wang, D., Hematite-based solar water splitting: Challenges and opportunities. *Energy Environ. Sci.* **2011,** *4*, 4862-4869.

20. Kennedy, J. H.; Frese Jr, K. W., Photo-oxidation of water at alpha -Fe_2O_3 electrode. *J. Electrochem. Soc.* **1978,** *125*, 709-714.

21. Sivula, K.; Zboril, R.; Le Formal, F.; Robert, R.; Weidenkaff, A.; Tucek, J.; Frydrych, J.; Grätzel, M., Photoelectrochemical water splitting with mesoporous hematite prepared by a solution-based colloidal approach. *J. Am. Chem. Soc.* **2010,** *132*, 7436-7444.

22. Liao, P.; Toroker, M. C.; Carter, E. A., Electron transport in pure and doped hematite. *Nano Lett.* **2011,** *11*, 1775-1781.

23. Pendlebury, S. R.; Barroso, M.; Cowan, A. J.; Sivula, K.; Tang, J.; Grätzel, M.; Klug, D.; Durrant, J. R., Dynamics of photogenerated holes in nanocrystalline α-Fe_2O_3 electrodes for water oxidation probed by transient absorption spectroscopy. *Chem. Commun.* **2011,** *47*, 716-718.

24. Xi, L.; Chiam, S. Y.; Mak, W. F.; Tran, P. D.; Barber, J.; Loo, S. C. J.; Wong, L. H., A novel strategy for surface treatment on hematite photoanode for efficient water oxidation. *Chem. Sci.* **2013,** *4*, 164-169.

25. Sivula, K.; Le Formal, F.; Grätzel, M., Solar water splitting: Progress using hematite (α-Fe_2O_3) photoelectrodes. *ChemSusChem* **2011,** *4*, 432-449.

26. Cherepy, N. J.; Liston, D. B.; Lovejoy, J. A.; Deng, H.; Zhang, J. Z., Ultrafast Studies of Photoexcited Electron Dynamics in γ- and α-Fe_2O_3 Semiconductor Nanoparticles. *J. Phys. Chem. B* **1998,** *102*, 770-776.

27. Sivula, K.; Le Formal, F.; Grätzel, M., Solar water splitting: Progress using hematite (α-Fe_2O_3) photoelectrodes. *ChemSusChem* **2011,** *4*, 432-449.

28. Grätzel, M., Photoelectrochemical cells. *Nature* **2001,** *414*, 338-344.

29. Peter, L. M.; Upul Wijayantha, K. G., Photoelectrochemical Water Splitting at Semiconductor Electrodes: Fundamental Problems and New Perspectives. *ChemPhysChem* **2014,** *15*, 1983-1995.

30. Bassi, P. S.; Gurudayal; Wong, L. H.; Barber, J., Iron based photoanodes for solar fuel production. *Phys. Chem. Chem. Phys.* **2014,** *16*, 11834-11842.

31. Ling, Y.; Wang, G.; Wheeler, D. A.; Zhang, J. Z.; Li, Y., Sn-doped hematite nanostructures for photoelectrochemical water splitting. *Nano Letters* **2011,** *11*, 2119-2125.

32. Liu, J.; Liang, C.; Zhang, H.; Zhang, S.; Tian, Z., Silicon-doped hematite nanosheets with superlattice structure. *Chem. Commun.* **2011,** *47*, 8040-8042.

33. Xi, L.; Tran, P. D.; Chiam, S. Y.; Bassi, P. S.; Mak, W. F.; Mulmudi, H. K.; Batabyal, S. K.; Barber, J.; Loo, J. S. C.; Wong, L. H., Co_3O_4-decorated hematite nanorods as

an effective photoanode for solar water oxidation. *J. Phys. Chem. C* **2012,** *116*, 13884-13889.

34. Iandolo, B.; Wickman, B.; Seger, B.; Chorkendorff, I.; Zorić, I.; Hellman, A., Faradaic efficiency of O_2 evolution on metal nanoparticle sensitized hematite photoanodes. *Phys. Chem. Chem. Phys.* **2014,** *16*, 1271-1275.

35. Ager, J. W.; Shaner, M. R.; Walczak, K. A.; Sharp, I. D.; Ardo, S., Experimental demonstrations of spontaneous, solar-driven photoelectrochemical water splitting. *Energy Environ. Sci.* **2015,** *8*, 2811-2824.

36. Etgar, L.; Gao, P.; Xue, Z.; Peng, Q.; Chandiran, A. K.; Liu, B.; Nazeeruddin, M. K.; Grätzel, M., Mesoscopic $CH_3NH_3PbI_3/TiO_2$ heterojunction solar cells. *J. Am. Chem. Soc.* **2012,** *134*, 17396-17399.

37. Gurudayal; Chee, P. M.; Boix, P. P.; Ge, H.; Yanan, F.; Barber, J.; Wong, L. H., Core–Shell Hematite Nanorods: A Simple Method To Improve the Charge Transfer in the Photoanode for Photoelectrochemical Water Splitting. *ACS Appl. Mater. Interf.* **2015,** *7*, 6852-6859.

38. Gurudayal; Chiam, S. Y.; Kumar, M. H.; Bassi, P. S.; Seng, H. L.; Barber, J.; Wong, L. H., Improving the Efficiency of Hematite Nanorods for Photoelectrochemical Water Splitting by Doping with Manganese. *ACS Appl. Mater. Interf.* **2014,** *6*, 5852-5859.

39. Lin, Y.; Yuan, G.; Liu, R.; Zhou, S.; Sheehan, S. W.; Wang, D., Semiconductor nanostructure-based photoelectrochemical water splitting: A brief review. *Chem. Phys. Lett.* **2011,** *507*, 209-215.

40. Dunn, H. K.; Feckl, J. M.; Muller, A.; Fattakhova-Rohlfing, D.; Morehead, S. G.; Roos, J.; Peter, L. M.; Scheu, C.; Bein, T., Tin doping speeds up hole transfer during light-driven water oxidation at hematite photoanodes. *Phys. Chem. Chem. Phys.* **2014,** *16*, 24610-24620.

41. Peter, L. M.; Wijayantha, K. G. U.; Tahir, A. A., Kinetics of light-driven oxygen evolution at α-Fe_2O_3 electrodes. *Faraday Discuss.* **2012,** *155*, 309-322.

42. Li, W.; He, D.; Sheehan, S. W.; He, Y.; Thorne, J. E.; Yao, X.; Brudvig, G. W.; Wang, D., Comparison of heterogenized molecular and heterogeneous oxide catalysts for photoelectrochemical water oxidation. *Energy Environ. Sci.* **2016,** *9*, 1794-1802.

43. Zachaus, C.; Abdi, F. F.; Peter, L. M.; van de Krol, R., Photocurrent of $BiVO_4$ is limited by surface recombination, not surface catalysis. *Chem. Sci.* **2017,** *8*, 3712-3719.

44. Gartner, W. W., Depletion-Layer Photoeffects in Semiconductors. *Phys. Rev.* **1959,** *116*, 84-87.

45. Peter, L. M.; Li, J.; Peat, R., Surface recombination at semiconductor electrodes. *J. Electroanal. Chem. Interf. Electrochem.* **1984,** *165*, 29-40.

46. Li, J.; Peter, L. M., Surface recombination at semiconductor electrodes. *J. Electroanal. Chem. Interf. Electrochem.* **1985,** *193*, 27-47.

47. Peter, L. M., Dynamic aspects of semiconductor photoelectrochemistry. *Chem. Rev.* **1990,** *90*, 753-769.

48. Ponomarev, E. A.; Peter, L. M., A generalized theory of intensity modulated photocurrent spectroscopy (IMPS). *J. Electroanal. Chem.* **1995,** *396*, 219-226.

49. Pihosh, Y.; Turkevych, I.; Mawatari, K.; Uemura, J.; Kazoe, Y.; Kosar, S.; Makita, K.; Sugaya, T.; Matsui, T.; Fujita, D.; Tosa, M.; Kondo, M.; Kitamori, T., Photocatalytic generation of hydrogen by core-shell $WO_3/BiVO_4$ nanorods with ultimate water splitting efficiency. *Sci. Rep.* **2015,** *5*, 11141.

50. Bassi, P. S.; Chiam, S. Y.; Gurudayal; Barber, J.; Wong, L. H., Hydrothermal Grown Nanoporous Iron Based Titanate, Fe_2TiO_5 for Light Driven Water Splitting. *ACS Appl. Mater. Interf.* **2014,** *6*, 22490-22495.

51. Peter, L. M.; Ponomarev, E. A.; Fermín, D. J., Intensity-modulated photocurrent spectroscopy: reconciliation of phenomenological analysis with multistep electron transfer mechanisms. *J. Electroanal. Chem.* **1997,** *427*, 79-96.

52. Fermín, D. J.; Ponomarev, E. A.; Peter, L. M., A kinetic study of CdS photocorrosion by intensity modulated photocurrent and photoelectrochemical impedance spectroscopy. *J. Electroanal. Chem.* **1999,** *473*, 192-203.

53. Klahr, B.; Gimenez, S.; Fabregat-Santiago, F.; Hamann, T.; Bisquert, J., Water Oxidation at Hematite Photoelectrodes: The Role of Surface States. *J. Am. Chem. Soc.* **2012,** *134*, 4294-4302.

54. Liao, P.; Carter, E. A., Hole transport in pure and doped hematite. *J. Appl. Phys.* **2012,** *112*, 013701, 1-13.

55. Gurudayal; Jeong, D.; Jin, K.; Ahn, H.-Y.; Boix, P. P.; Abdi, F. F.; Mathews, N.; Nam, K. T.; Wong, L. H., Highly Active MnO Catalysts Integrated onto Fe_2O_3 Nanorods for Efficient Water Splitting. *Adv. Mater. Interf.* **2016,** *3* (15), 1600176, 1-7.

56. Parmar, K. P. S.; Kang, H. J.; Bist, A.; Dua, P.; Jang, J. S.; Lee, J. S., Photocatalytic and Photoelectrochemical Water Oxidation over Metal-Doped Monoclinic $BiVO_4$ Photoanodes. *ChemSusChem* **2012,** *5* (10), 1926-1934.

57. Kim, J. Y.; Jun, H.; Hong, S. J.; Kim, H. G.; Lee, J. S., Charge transfer in iron oxide photoanode modified with carbon nanotubes for photoelectrochemical water oxidation: An electrochemical impedance study. *Int. J. Hydrogen Energy* **2011,** *36* (16), 9462-9468.

58. Su, J.; Wang, J.; Liu, C.; Feng, B.; Chen, Y.; Guo, L., On the role of metal atom doping in hematite for improved photoelectrochemical properties: a comparison study. *RSC Adv.* **2016,** *6* (104), 101745-101751.

59. Park, H. S.; Kweon, K. E.; Ye, H.; Paek, E.; Hwang, G. S.; Bard, A. J., Factors in the metal doping of $BiVO_4$ for improved photoelectrocatalytic activity as studied by scanning electrochemical microscopy and first-principles density-functional calculation. *J. Phys. Chem. C* **2011,** *115* (36), 17870-17879.

60. Lunt, R. A.; Jackson, A. J.; Walsh, A., Dielectric response of Fe_2O_3 crystals and thin films. *Chem. Phys. Lett.* **2013,** *586,* 67-69.

TOC Graphic
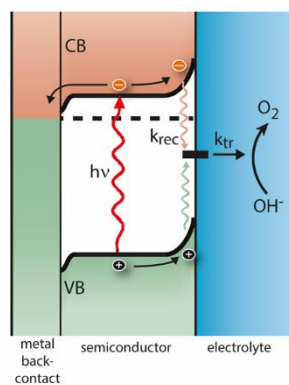
Intensity modulated photocurrent spectroscopy was used to reveal the enhancement mechanism in hematite nanorods. Although the photo-electrochemical enhancement of various modifications to photoelectrodes may be similar, the effect on surface carrier dynamics can be very different.